Ceramics International 47 (2021) 24860–24867

Contents lists available at ScienceDirect

Ceramics International

journal homepage: www.elsevier.com/locate/ceramint

Interfacial segregation in Cl^--doped nano-ZnO polycrystalline semiconductors and its effect on electrical properties

Gustavo M. Fortes [a,*], Andre L. da Silva [a], Lorena B. Caliman [a], Fabio C. Fonseca [b], Douglas Gouvêa [a]

[a] Department of Metallurgical and Materials Engineering, Polytechnic School - University of São Paulo, São Paulo, 05508-030, Brazil
[b] Instituto de Pesquisas Energéticas e Nucleares, IPEN-CNEN/SP, São Paulo, 05508000, Brazil

ARTICLE INFO

Keywords:
Semiconductors
Space charge layer
ZnO
Interfacial segregation
Electrical properties

ABSTRACT

In this study, interfacial segregation in Cl^--doped ZnO (0.0, 1.0, 3.0, 4.0, and 6.0 mol%) was explored as a strategy to compensate the space charge layer to decrease the electric potential barrier height at the grain boundaries and increase the overall electrical conductivity of the system. The focus of this work was to evaluate the dopant segregation and provide the first insights into the influence of interfacial segregation on the electrical properties. By using a systematic lixiviation method, we demonstrated that in addition to the bulk solubility, the Cl^- anions segregated at both the surface and grain boundaries. Impedance spectroscopy measurements showed a four orders of magnitude reduction in the total electrical resistivity in the Cl^--doped ZnO samples compared to that of undoped ZnO. The calculated value of the electric potential barrier height decreased, as well as the activation energy for conduction, which decreased from 853 meV for undoped ZnO to 168 meV for 1.2 mol% Cl^--doped ZnO.

1. Introduction

Polycrystalline semiconductors are a relevant class of technological materials widely used as low-resistance electrodes, as well as in thin-film transistors, solar cells, photocatalysis, artificial photosynthesis, and thermoelectric (TE) devices [1]. These materials are composed of micro/nanocrystallites joined by grain boundaries (GBs), which consist of a few atomic layers of disordered atoms caused by the misorientation of the lattice between grains. GBs typically present several crystallographic defects, such as dislocations, vacancies, interstitials, dangling bonds, and distorted bond angles. These irregularities lead to the formation of electronic states, which may have energy levels within the band gap and act as intraband gap trap centers for charge carriers [2,3]. GBs can exhibit an electron-depletion layer that induces an electric potential across the barrier, which controls the charge-carrier mobility. Thus, the properties of the GB region play a crucial role in controlling the charge transport properties of polycrystalline materials [2].

The electric potential barrier at the GBs is typically described by a model used for metal oxide varistor systems [4,5]. Electrons flow into the GBs until the Fermi level reaches the same value throughout the entire material. In the GBs, these electrons are trapped by defects, creating a negative charge at the boundary. Because local electrical neutrality must be maintained, a depletion layer, positively charged, forms on both sides of the GB. These layers create an electrostatic field in the form of a boundary barrier, which is known as a double Schottky barrier (DSB) [4,5]. The electric potential barrier at the GBs prevents the transport of electrons (e^-) and holes (h^+) from one grain to the next. It also reduces the band gap and increases coupling [6], which leads to charge recombination [4,6,7].

Zinc oxide (ZnO) is an interesting polycrystalline semiconductor. Undoped ZnO is an intrinsic n-type semiconductor. Electrons are the main charge carriers because of the formation of oxygen vacancies ($V_O^{\cdot\cdot}$) ($O_O^\times = 1/2O_2(g) + V_O^{\cdot\cdot} + 2e'$) and interstitial zinc ($Zn_i^{\cdot\cdot}$) ($Zn_{Zn}^\times + O_O^\times = Zn_i^{\cdot\cdot} + 2e' + 1/2O_2(g)$) [8–11]. The electronic configuration of wurtzite (the most common phase of ZnO) leads to a direct band gap, where the valence band (VB) maximum and conduction band (CB) minimum are aligned with the same crystal momentum; thus, only a photon is required to make the interband transition [12]. Many applications of ZnO-based compounds are driven by the transport of electrons and holes throughout the material. For instance, $Cu/ZnO/Al_2O_3$ catalysts have been used for methanol production since 1960 [13]. Pure ZnO can also be used to produce methanol using CO_2 and H_2O as precursors [14].

---

* Corresponding author.
E-mail address: gustavmf1@gmail.com (G.M. Fortes).

https://doi.org/10.1016/j.ceramint.2021.05.212
Received 18 January 2021; Received in revised form 13 May 2021; Accepted 20 May 2021

The electrical conductivity of ZnO is one of the main properties influencing the use of ZnO as a semiconductor material. The electrical properties have been modified by dopants such as Co, Ni, In, Ga, Sn, and Cl^- [15–19]. Cl^- doping has shown a pronounced increase in electrical conductivity, reaching five orders of magnitude higher than that of undoped ZnO [20]. Structurally, Cl^- (0.181 nm ionic radius) is known to replace O^{2-} (0.140 nm ionic radius) in the lattice [8,21–23], causing lattice expansion owing to its larger ionic radius [22,24]. Typically, the solubility of Cl^- in bulk ZnO has been thought to be the main reason for the increased electrical conductivity. However, a more detailed investigation of possible Cl^- segregation at ZnO interfaces is still lacking.

Interfacial segregation is driven by the enthalpy of segregation (ΔH_{seg}), which, in crystalline systems, is associated with four types of driving forces: (i) the difference in surface energy between the doping oxide and the host (ΔH_γ), (ii) an elastic solute strain energy due to the size difference between the dopant and host ions (ΔH_ε), (iii) solute–solvent interactions (ΔH_ω), and (iv) electrostatic potential/charge compensation (ΔH_φ). Thus, ΔH_{seg} can be expressed as shown in eq. (1) [25].

$$\Delta H_{seg} = \Delta H_\gamma + \Delta H_\varepsilon + \Delta H_\omega + \Delta H_\varphi \tag{1}$$

The difference in the surface energy (ΔH_γ) is described by eq. (2), where γ_1 and γ_2 are the surface energies of the solute and solvent, respectively, and A is the surface area. The elastic strain in the system (ΔH_ε) depends on the difference between the ionic radii of the solute (r_1) and the solvent (r_2) according to eq. (3), where G is the stiffness modulus, and K is the compressive modulus. The solute–solvent interaction (ΔH_ω) depends on the heat of mixing (ΔH_m), where Z^* is the solute fraction on the surface of the solvent, and X_1 and X_2 are the molar fractions of the solvent and solute in the bulk, respectively (eq. (4)). Finally, the electrostatic potential and charge compensation (ΔH_φ) are presented in eq. (5), where q is the product of the ion charges, e is the electron charge, and φ_∞ is the electrical potential in the depletion layer [25].

$$\Delta H_\gamma = (\gamma_2 - \gamma_1)\,A \tag{2}$$

$$\Delta H_\varepsilon = \frac{24\pi K G r_1 r_2 (r_1 r_2)^2}{4Gr_1 + 3Kr_2} \tag{3}$$

$$\Delta H_{seg} = \frac{\Delta H_m}{Z^* X_1 X_2} \tag{4}$$

$$\Delta H_{seg} = -q e \varphi_\infty \tag{5}$$

Although it is difficult to precisely predict if a dopant will segregate on the surface and/or in the GBs, based on eqs. (2)–(5) and considering some key differences between chloride and oxygen (such as ionic radius and electronegativity), it can be argued that chloride will likely segregate to the ZnO interfaces. The amount of dopant that segregates at each interface is still difficult to estimate. However, from a thermodynamic viewpoint, the additive (dopant) should segregate at the interface with higher energy to minimize the overall energy of the system. Thus, when Cl^- is doped into ZnO, it is expected that it will segregate on both the surface (solid–gas interface) and at GBs, which could potentially impact the electric potential barrier and change the overall electrical conductivity of the system. Therefore, the present study aims to unravel the Cl^- segregation in ZnO by quantifying the dopant excess on the surface and GBs and determining the relationship between segregation and the electrical properties of Cl^--doped ZnO.

2. Experimental procedure

2.1. Synthesis of Cl^--doped ZnO nanopowders

ZnO nanopowders were synthesized using the polymeric precursor method [26]. The process used 45.8 wt% anhydride citric acid (Synth, $C_6H_8O_7$, ≥99.00 wt% purity), 30.5 wt% ethylene glycol (Synth, $C_2H_6O_2$, ≥99.00 wt% purity), and 23.6 wt% hydrated zinc nitrate (Synth, $Zn(NO_3)_2{\cdot}6H_2O$, ≥ 99.98 wt% purity), which was used as zinc source. Dissolution was conducted at 70 °C until complete homogeneity and transparency were achieved. Then, the solution was heated to 120 °C for polymerization and elimination of volatiles, such as NO_x and H_2O, from the nitrates. Chloride was introduced by adding calculated amounts of an NH_4Cl (Synth, ≥ 99.50 wt% purity) aqueous solution to the resin.

The target molar concentrations of Cl^- were $x = 0.0\%$, 1.0%, 3.0%, 4.0%, and 6.0%. The corresponding samples used in this study are labeled as ZnOCl-*x*. Calcination was conducted in two steps. First, to decompose the organic resin, each sample was held at 360 °C under excess air for 5 h. Then, the powders were manually ground with a mortar and pestle and heated to 360 °C for 15 h under air flow to complete the oxidation and stabilized the particle size.

2.2. Powder characterization

The Cl^- content in each sample was measured using a chloride-selective electrode (Hanna Instruments). The prepared powders were dissolved in a 1 N sulfuric acid solution and further neutralized with a 2 M potassium hydroxide solution to adjust the pH of the electrode to the operational range.

X-ray diffraction (XRD) patterns were obtained using an X'Pert-MPD (Philips) diffractometer with Cu Kα radiation, operated at 45 kV and 40 mA. The step size was set at 0.02° 2θ per second over the 5–70° 2θ range. The crystallite sizes and lattice parameters were calculated by Rietveld analysis using the X'Pert Highscore software with $MgAl_2O_4$ as the standard.

The powder density was measured using a Micromeritics AccuPyc II 1340 He gas pycnometer after 200 purges for degassing. The specific surface areas of the samples were determined by nitrogen gas adsorption at 77 K (Micromeritics Gemini III 2375) according to the Brunauer–Emmett–Teller (BET) method. The samples were degassed before the experiment at 300 °C for ~12 h using a VacPrep 061 (Micromeritics).

The morphology of the powders was analyzed using transmission electron microscopy (TEM) with a JEM-2100 (JEOL) microscope operated with a parallel beam at 200 kV equipped with a 4k × 4k (TVIPS) camera.

2.3. Surface segregation and electrical characterization

The amount of Cl^- that segregated on the surface of the ZnO nanoparticles was determined using the selective lixiviation method [25, 27–30]. The procedure was performed by ultrasonicating ~100 mg of powder with ~1.8 g of distilled water for 1 h. The supernatant and powder were separated by centrifuging twice at 13,000 rpm (10,390 G) for 1 h. Then, approximately 1 g of the supernatant solution was collected, and the Cl^- content was measured using the chloride-selective electrode.

Impedance spectroscopy (IS) measurements were performed using an impedance meter and gain-phase analyzer (Solartron 1260). The specimens were prepared by pressing (125 MPa) the powders into 5 mm × 11 mm (diameter) cylindrical pellets. The pressed samples were then treated at 370 °C for 1 h to enhance the grain boundary area. The objective was not to obtain a sintered pellet but a pressed sample that enabled the measurement of the electrical properties of the as-prepared nanopowders. Because dopant segregation was the focus of this study, IS was used as a tool to determine the relationship between interfacial segregation and the electrical properties of a polycrystalline semiconductor for the first time. We focused on the total electrical resistivity without the challenging task of deconvolving the IS curves of highly porous samples. The IS data were collected in the frequency range of 3×10^7 to 1 Hz with an AC voltage amplitude of 500 mV and zero DC bias. High-purity silver paste, cured at room temperature, was used to prepare the electrodes in the Ag/Cl–ZnO/Ag symmetric cell configuration. The IS sample holder, with platinum leads and a type-K thermocouple positioned close to three samples measured at the same temperature, was inserted in an alumina tube placed in a resistive tube furnace under a controlled atmosphere [31]. The samples were heated to 200 °C under a steady flux (~50 mL/min) of synthetic dry air to ensure the desorption of most of the H_2O and CO_2 from the sample. The flux of synthetic dry air was kept constant, and the IS data were measured upon cooling at 200, 150, and 100 °C. Before the IS measurements, the samples were maintained for ~30 min at each measuring temperature to allow thermal equilibration. The total electrical conductivity was determined by fitting the IS diagrams normalized by the geometric factors of the samples.

3. Results and discussion

3.1. Powder characterization

The XRD patterns of the undoped ZnO and Cl^--doped ZnO samples are shown in Fig. 1. Broad peaks can be observed, which are typical of nanosized crystallites. Wurtzite (JCPDS card no. 36–1451) was the only phase identified, indicating single-phase samples.

The average crystallite size, lattice parameters, and unit cell volumes of the undoped and doped ZnO are listed in Table 1. The crystallite sizes exhibited no clear dependence on Cl^- doping. This behavior is different from previous observations of crystallite size dependence on cation dopants in nano-oxides [25,28,32–43]. A small decrease in the crystallite size was observed for the ZnOCl-3 and ZnOCl-4 samples. In contrast, the lattice parameters increased slightly with increasing Cl^- content. This expansion of the unit cell volume may be an indication of a solid solution or surface energy reduction. According to the Young–Laplace equation (eq. (6)), a decrease in the surface energy (γ) for crystallites of radius (r) reduces the effective pressure (P) over the crystallite, allowing its lattice to expand [44,45].

$$P = \frac{2\gamma}{r} \tag{6}$$

The Cl^- contents in the ZnO nanopowders obtained using the selective electrode are presented in Table 1. The amount of Cl^- retained in the sample was considerably lower than the target composition. The lower amount of Cl^- was probably due to evaporation losses during calcination. The samples with a higher target composition had a higher amount of retained Cl^-. However, the percentage of dopant retained decreased systematically. The amounts of Cl^- remaining in the samples, compared to the target values, were 37%, 27%, 25%, and 20% for ZnOCl-1, ZnOCl-3, ZnOCl-4, and ZnOCl-6, respectively. The undoped sample also presented traces of Cl^-, which was due to the intrinsic contamination of the precursors used in the ZnO synthesis.

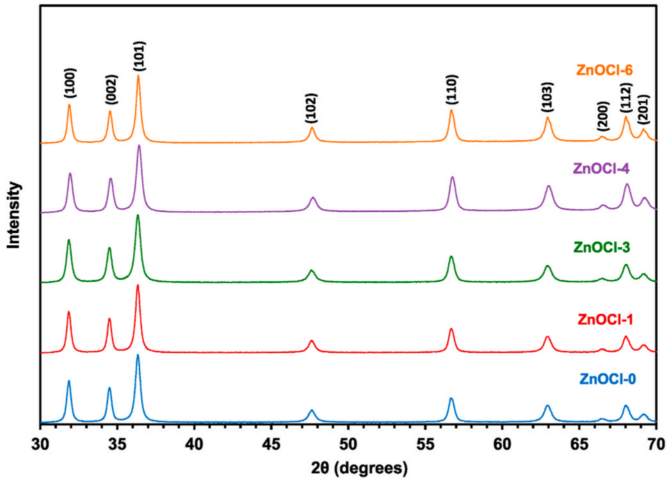

Fig. 1. XRD patterns of ZnO and Cl^--doped ZnO.

Table 1
Cl^- content, crystallite sizes, and lattice parameters of undoped and Cl^--doped ZnO nanopowders.

Sample	Cl^- (mol %)	Crystallite size (nm)	Lattice parameter a (Å)	Lattice parameter c (Å)	Unit cell volume (Å^3)
ZnOCl-0	0.07 ± 0.01	27.50 ± 0.50	3.2504 ± 0.0002	5.2098 ± 0.0003	47.6678 ± 0.0057
ZnOCl-1	0.37 ± 0.03	29.11 ± 0.24	3.2505 ± 0.0002	5.2098 ± 0.0003	47.6708 ± 0.0057
ZnOCl-3	0.80 ± 0.07	24.65 ± 0.33	3.2505 ± 0.0002	5.2106 ± 0.0004	47.6781 ± 0.0066
ZnOCl-4	0.98 ± 0.09	24.71 ± 0.43	3.2513 ± 0.0005	5.2116 ± 0.0005	47.7107 ± 0.0119
ZnOCl-6	1.23 ± 0.11	28.71 ± 0.49	3.2519 ± 0.0004	5.2114 ± 0.0005	47.7265 ± 0.0104

The increase in the unit cell volume may be related to the bond length. Stoichiometric ZnO has a Zn–O distance of 1.97 Å, while the Zn–Cl distance (doped samples) is ~2.40 Å. This is a consequence of a larger ionic radius of Cl^- (1.81 Å) compared to that of O^{2-} (1.40 Å), which is replaced by Cl^- in the ZnO lattice [24,46].

The density, specific surface area (SSA), total specific area (TSA), specific grain boundary (SGB) area, and SGB/SSA ratio are listed in Table 2. Apart from the ZnOCl-1 sample, the measured density decreased as the amount of Cl^- increased. The decreased apparent density might be associated with the creation of point defects such as zinc vacancies (V''_{Zn}) [47], which could be induced by Cl^- replacing O^{2-} to maintain electroneutrality.

The SSA, measured by gas adsorption, increased as the crystallite size decreased, as expected. It decreased for small doping of Cl^- (ZnOCl-1), followed by an increase for ZnOCl-3 and ZnOCl-4, and finally decreased for the ZnOCl-6 sample. The TSA was calculated according to eq. (7) by assuming a truncated octahedron shape, where d is the average crystallite size, and ρ is the measured density [49]. The SGB area, which is the difference between the TSA and SSA divided by two, was calculated according to eq. (8).

$$TSA = \frac{7.11}{d \cdot \rho} \tag{7}$$

$$SGB = \frac{(TSA - SSA)}{2} \tag{8}$$

The TSA and SGB presented similar behavior with respect to the amount of Cl^-, following the trend observed for the SSA. The SGB/SSA ratio was essentially constant for all studied compositions, which suggests that the structure maintained a balance between the interfacial

Table 2
Density, specific surface area, total specific area, specific grain boundary area, and GB/SSA ratio. Theoretical density of ZnO is 5.673 g/cm^3 [48].

Sample	Density (g/cm^3)	SSA (m^2/g)	TSA (m^2/g)	SGB (m^2/g)	SGB/SSA
ZnOCl-0	5.632 ± 0.003	15.3 ± 0.1	46.5 ± 0.9	15.6 ± 1.0	1.02 ± 0.08
ZnOCl-1	5.645 ± 0.005	14.0 ± 0.1	43.7 ± 0.4	14.8 ± 0.5	1.06 ± 0.04
ZnOCl-3	5.526 ± 0.004	18.0 ± 0.1	52.7 ± 0.7	17.4 ± 0.8	0.96 ± 0.06
ZnOCl-4	5.423 ± 0.009	17.0 ± 0.1	53.0 ± 1.0	18.0 ± 1.1	1.06 ± 0.09
ZnOCl-6	5.281 ± 0.009	15.3 ± 0.1	46.8 ± 0.9	15.8 ± 1.0	1.03 ± 0.08

areas. This is an indication of an equilibrium between the GB energy and the surface energy, which is the first evidence that both interfaces are modified in the same way by dopant segregation.

The grain size, crystallinity, and morphology of the Cl$^-$-doped ZnO were analyzed using TEM (Fig. 2). The ZnOCl-3 sample was chosen for TEM observation because of its higher SSA and smaller crystallite size. The images reveal grains with irregular shapes, mostly rounded edges, and some hexagonal geometry, which overlay one another, forming agglomerates. The grains visually resemble the ~25 nm average size of the XRD data (Table 1). Fig. 2(b) shows some larger crystallites (~40–50 nm), emphasizing the grain boundary shared by two grains. Previous reports have shown that Cl$^-$ doping may shift the morphology of crystallites from a long hexagonal needle or equiaxed particles to hexagonal disks [21]. However, the TEM images showed that Cl$^-$ doping, in the studied range, had no appreciable effect on the particle shape when compared to the previous report of undoped nano-ZnO prepared by the polymeric precursor method [50]. It is likely that the synthesis method used in this work was the main reason the particle morphology did not change.

3.2. *Interfacial segregation and electrical characterization*

The interface excess (Γ) was calculated by measuring the total amount of Cl$^-$ in each sample and the amount of Cl$^-$ lixiviated from the ZnO surface. The surface excess (Γ_{Cl}^{S}) is given by eq. (9).

$$\Gamma_{Cl}{}^{S} = \frac{n_{Cl}{}^{S}}{SSA} \tag{9}$$

where n_{Cl}^{S} is the number of moles of Cl$^-$ lixiviated from the sample (Table 2). The GB excess (Γ_{Cl}^{GB}) can be calculated using eq. (10).

$$\Gamma_{Cl}{}^{GB} = \frac{n_{Cl}{}^{T} - n_{Cl}{}^{S} - n_{Cl}{}^{bulk}}{SGB} \tag{10}$$

where $n_{Cl}{}^{T}$ is the total amount of Cl$^-$ per gram of powder in the sample, and n_{Cl}^{bulk} is the bulk solubility.

While $n_{Cl}{}^{T}$ and n_{Cl}^{S} can be directly measured by chemical analysis, n_{Cl}^{bulk} must be estimated. The Cl$^-$ bulk solubility was determined based on thermodynamic evidence, as follows.

As observed in Table 2, the SGB/SSA ratio was independent of Cl$^-$ doping. According to eq. (11) [32,51–53], the interfacial area variation (dA_i) is related to the interfacial energy (γ_i), and the product of the two is given by the Gibbs free energy variation (dG), which governs the nanostability of a system at constant composition (n), pressure (P), and temperature (T).

$$dG = \sum (\gamma_i dA_i)_{T,P,n} \tag{11}$$

The main driving force for grain growth on nano-oxides is related to the decrease in Gibbs free energy, which is also related to the reduction in the specific interfacial area at a given temperature [32]. In this system, the unchanged SGB/SSA ratio throughout the samples suggests that the interfacial energy ratio (γ_{GB}/γ_S) was also constant. Thus, based on eq. (12), which relates the interfacial energies (surface and GB) to the excesses, it is possible to write eq. (13).

$$\gamma = \gamma_0 + \Gamma\cdot\Delta H_{seg} \tag{12}$$

$$\frac{(\gamma^{GB} - \gamma_0{}^{GB})}{(\gamma^{S} - \gamma_0{}^{S})} = \frac{\Gamma^{GB}\cdot\Delta H_{seg}{}^{GB}}{\Gamma^{S}\cdot\Delta H_{seg}{}^{S}} \tag{13}$$

where γ^{GB} and $\gamma_0{}^{GB}$ are the GB energies with and without solute segregation, respectively, Γ^{GB} is the GB excess, and ΔH_{seg}^{GB} is the enthalpy of GB segregation. The denominator represents the same parameters for the solid–vapor interface (surface). This equation suggests that at a given temperature, the enthalpy of segregation ratio ($\Delta H_{seg}^{GB}/\Delta H_{seg}^{S}$) is constant, which leads to a direct proportionality between γ_{GB}/γ_S, $\Gamma_{Cl}^{GB}/\Gamma_{Cl}^{S}$, and SGB/SSA [25]. Considering this thermodynamic relation, we found that

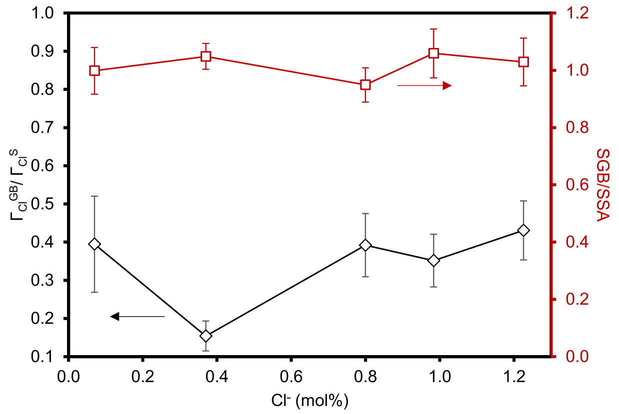

Fig. 3. Optimal calculated $\Gamma_{Cl}^{GB}/\Gamma_{Cl}^{S}$ ratio and SGB/SSA ratio plotted against the total amount of Cl$^-$.

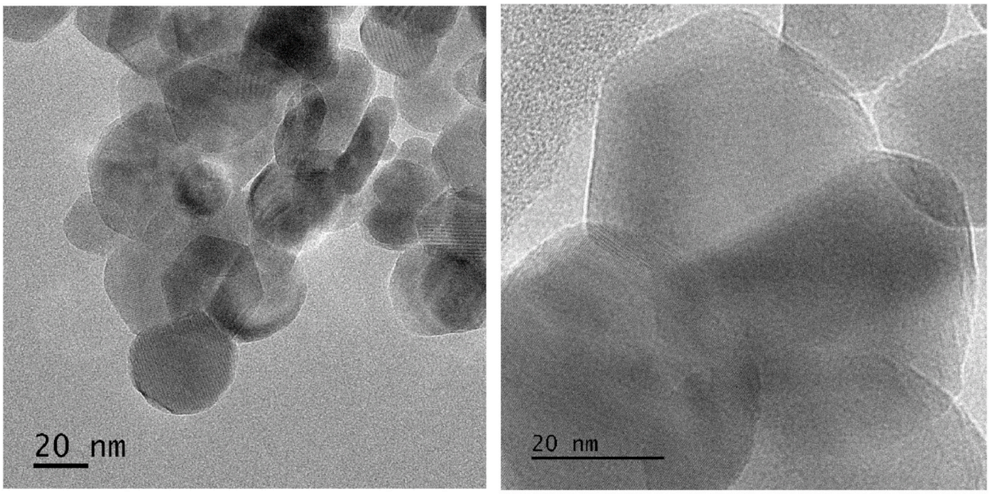

(a) (b)

Fig. 2. TEM images of the ZnOCl-3 sample. (a) Equiaxed and hexagonal crystallites, and (b) highlight of a grain boundary shared by two grains.

the $\Gamma_{Cl}^{GB}/\Gamma_{Cl}^{S}$ ratio became stable at higher Cl^- doping. The stable $\Gamma_{Cl}^{GB}/\Gamma_{Cl}^{S}$ ratio was found to be ~0.4, as shown in Fig. 3. From this optimal ratio, the Cl^- bulk solubility (n_{Cl}^{bulk}) was estimated to be 0.016 mol%. Thus, this value was used to calculate Γ_{Cl}^{GB} (eq. (10)).

The dependence of the surface and GB excess on Cl^- content are shown in Fig. 4 and Table 3. Both the surface and GB excess increased systematically as the Cl^- content increased. However, the surface excess was higher than the GB excess for all the compositions.

Fig. 5 shows the IS diagrams measured at 150 °C for the undoped and Cl^--doped ZnO pellets of pressed nanoparticles. Typically, IS data are composed of multiple semicircular arcs representing the relaxations of various microstructural components in the material, such as grains, grain boundaries, and other blocking interfaces (such as pores and insulating phases), along with possible electrode polarization. However, in Fig. 5, all samples display a single semicircular arc, which is typically ascribed to charge-carrier blocking at grain boundaries and pores [10, 54–56], the primary resistive interface continuously connecting the solid pellets. The low-frequency contribution dominates and overlaps with other possible microstructural features, forming a single irregular semicircular arc. The main outcome is a striking decrease in the electrical resistivity upon Cl^- doping. Considering that the samples had similar porosities (~46.6 ± 3.5 vol%) and were carefully prepared under the same experimental conditions to minimize adsorbed species in the porous structure of the samples, such a pronounced decrease in the resistivity is mainly related to the effect of Cl^- doping.

The total electrical resistivity (ρ_e) obtained from the IS experiment at 150 °C (Fig. 5) and the calculated electrical conductivity (σ) are listed in Table 3. From Fig. 5, the intersection of the semicircular plot with the x-axis Z' at low frequencies represents the overall resistivity (ρ_e) of the samples. As ρ_e decreased, σ substantially increased with increasing Cl^- doping in the samples.

The increase in electrical conductivity in doped semiconductors is typically associated with an increase in the number of charge carriers (*N*). In the case of Cl^--doped ZnO, it is typically considered that Cl^- will form a solid solution with ZnO by substituting for O^{2-} and generating one electronic charge carrier, which would make the increase in the electrical conductivity proportional to the increase in *N*. The electrical conductivity (σ) is defined by the number of charge carriers, their mobility (μ), and their charge ($|e10^{-19} \times 1.6 = |$ C, for electrons), according to eq. (14) [57].

$$\sigma = N\,\mu\,|e| \tag{14}$$

Table 3
Surface excess (Γ_{Cl}^{S}), GB excess (Γ_{Cl}^{GB}), resistivity (ρ_e) obtained from the impedance tests and calculated electrical conductivity (σ) for undoped and Cl^--doped ZnO nanoparticles. For the IS tests, the porosity of the pellets was kept constant (~41–50 vol%).

Sample	Cl^- (mol %)	Γ_{Cl}^{S} (μmol/m^2)	Γ_{Cl}^{GB} (μmol/m^2)	ρ_e (Ω·m)	σ ($\Omega^{-1}\cdot m^{-1}$)
ZnOCl-0	0.07 ± 0.01	0.30 ± 0.02	0.12 ± 0.03	133,491	7.5×10^{-6}
ZnOCl-1	0.37 ± 0.03	2.66 ± 0.22	0.41 ± 0.07	7,566	1.3×10^{-4}
ZnOCl-3	0.80 ± 0.07	3.95 ± 0.32	1.55 ± 0.20	328	3.0×10^{-3}
ZnOCl-4	0.98 ± 0.09	5.13 ± 0.44	1.80 ± 0.20	114	8.8×10^{-3}
ZnOCl-6	1.23 ± 0.11	6.77 ± 0.59	2.92 ± 0.27	72	1.4×10^{-2}

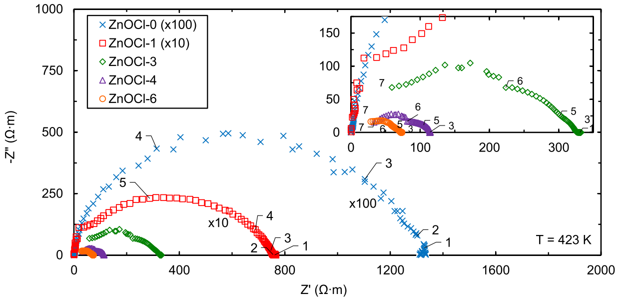

Fig. 5. Impedance spectroscopy diagrams of Cl^--doped ZnO pellets measured at 150 °C. Numbers indicate the logarithm of the frequency.

Assuming that each Cl^- in the lattice generates a charge carrier, *N* should increase proportionally to the total amount of Cl^- in the doped samples. Consequently, the electrical conductivity should increase proportionally. To determine if this proportionality applies to the present system, the increase in charge carriers was calculated by assuming that each Cl^- generates one mobile electron–hole pair. This increment was compared to the observed increase in electrical conductivity, as shown in Table 3. A comparison between the measured increase in σ and the expected increase due to the increase in charge carriers (*N*) is presented in Fig. 6.

According to Fig. 6, the increase in electrical conductivity measured in the samples significantly surpasses a possible increase due to the number of charge carriers that would be added to the system if each Cl^- increased *N* by one. The substitution of O^{2-} by Cl^- introduces a shallow donor state derived from Cl 3s states [23]. In such a case, the *N* in the system to fit the electrical conductivity expectations associated with the bulk properties (eq. (14)) would be 1 N, 8 N, 55 N, 134 N, and 156 N for the ZnOCl-0, ZnOCl-1, ZnOCl-3, ZnOCl-4, and ZnOCl-6 samples,

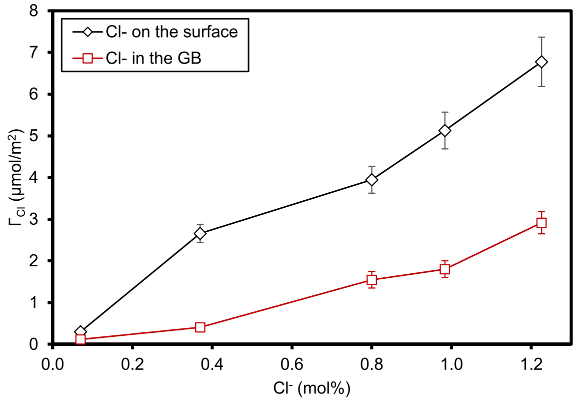

Fig. 4. Surface and GB excess plotted against the total amount of Cl^- in the ZnO nanoparticles.

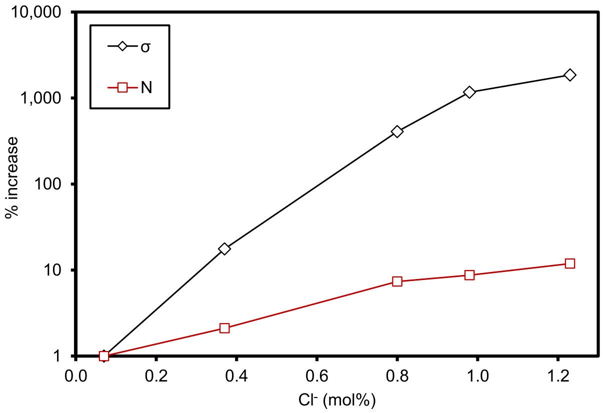

Fig. 6. Relative increase (%) in electrical conductivity (σ) and the number of charge carriers (*N*) versus the total amount of Cl^-.

respectively. However, the results obtained from the calculations suggest that this phenomenon is not associated with the bulk doping effect.

Therefore, the increase in electrical conductivity was possibly caused by GB modification. To examine the relationship between the total amount of Cl^- and the calculated GB excess with the electrical conductivity, Fig. 7 is presented.

From Fig. 7, it is observed that the increase in electrical conductivity, plotted against the total amount of Cl^-, matches the increase in the GB excess. These data suggest that GB segregation plays a crucial role in this matter. The significant improvement in the electrical conductivity by four orders of magnitude (1,857 times) cannot be explained by the promotion of more electrons in the CB, as shown in Fig. 6.

In polycrystalline materials, the grain boundary acts as a barrier that prevents electrons from moving freely throughout the sample. This barrier is known as the space charge layer, which is associated with the electric potential barrier height (ϕ_B). ϕ_B can be calculated when no external voltage bias is applied (V = 0) using eq. (15) [4,5].

$$\phi_B = \frac{|e|^2 d^2 N_d}{2\varepsilon_0 \varepsilon_r} \tag{15}$$

where $|e|$ is the modulus of the electron charge (1.6×10^{-19} C), ε_0 is the permittivity of free space (8.85×10^{-12} F/m), ε_r is the relative permittivity ($\varepsilon_r = 8.5$ for ZnO [58]), and N_d is the charge carrier concentration within the electron depletion layer of thickness d, which, for relative calculations, was assumed to be 1 nm in the present system. The determination of N_d was not possible, but considering that each Cl^- from the Γ_{Cl}^{GB} could cancel one positive charge [4], how the variation in N_d (ΔN_d) from the undoped sample (ZnOCl-0) relative to the doped ones could cause a variation in the electric potential barrier height ($\Delta\phi_B$) was determined according to eq. (16).

$$(\Delta\phi_B) = \frac{|e|^2 d^2 (\Delta N_d)}{2\varepsilon_0 \varepsilon_r} \tag{16}$$

Fig. 8 shows the decrease in $\Delta\phi_B$ relative to ZnOCl-0, plotted as a function of the volumetric concentration of Cl^- at the GB. Although the initial electric potential barrier, ϕ_{B0}, of the undoped ZnO (ZnOCl-0) was not determined, it decreased linearly with increasing amount of Cl^- at the GB. This behavior suggests that Γ_{Cl}^{GB} plays a decisive role in decreasing ϕ_B and, consequently, increasing the electrical conductivity. The potential barrier height of ZnO has been reported to be 530–800 meV at temperatures up to 400 °C [59,60]; thus, the reduction of 595 meV (ZnOCl-6) observed in this study is noteworthy, representing at least a 75% decrease in the potential barrier height.

To further understand the increase in the overall electrical conductivity, the activation energy for conduction was estimated according to the Arrhenius equation (eq. (17)) [61].

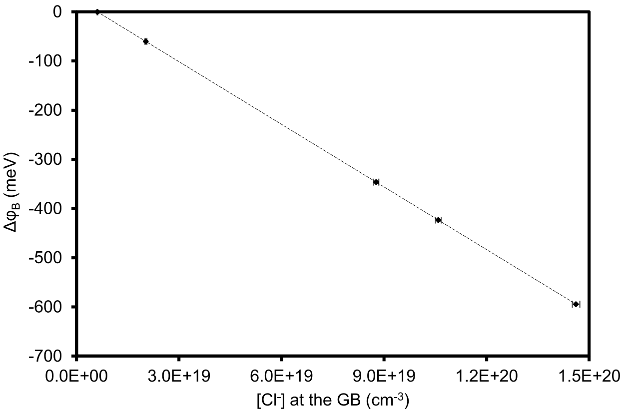

Fig. 8. Dependence of the electric potential barrier on the Cl^- concentration at the GB of undoped and Cl^--doped ZnO.

$$\ln\sigma = \ln\sigma_0 + \frac{1}{T}\left(\frac{-E_a}{R}\right) \tag{17}$$

where σ_0 is the intrinsic conductivity (S/cm), T is the absolute temperature (K), R is the ideal gas constant (0.0000862 eV/K), and E_a is the activation energy (meV).

The calculated E_a as a function of the amount of Cl^- in each sample is shown in Fig. 9. It is observed that E_a decreased linearly as the amount of Cl^- doping increased. The calculated E_a decreased from 853 meV (undoped ZnO) to 168 meV (1.2 mol% Cl^--doped ZnO). The value for undoped ZnO agrees with the range reported in the literature. Lee et al. [10] reported the E_a of pure ZnO as 570 meV for crystallite sizes of ~60 nm, while Godarvati et al. [62] recently reported an E_a of 1,081 meV for crystallite sizes of ~40 nm. The reduction of 685 meV in the E_a from undoped to 1.2 mol% Cl^--doped ZnO agrees with the 595 meV reduction in ϕ_B calculated at an intermediate temperature (150 °C) instead of the three temperatures (200, 150, and 100 °C) used to calculate the E_a. The equivalent magnitude of these values reinforces that the pronounced improvement in the overall electrical conductivity was primarily due to the segregation of Cl^- at the GBs, which reduced ϕ_B. Significant changes in the activation energy can be attributed to the different transport mechanisms or different charge carriers activated in the material. However, given that ZnO is an n-type semiconductor, the relatively low temperature range presented in this study (100–200 °C), and the observed correlation with ϕ_B, it is clear that the conductivity is

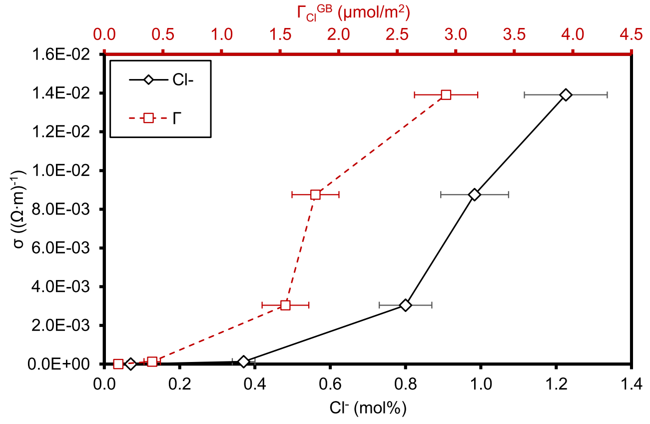

Fig. 7. Amount of Cl^- doping and GB excess in ZnO plotted against the electrical conductivity.

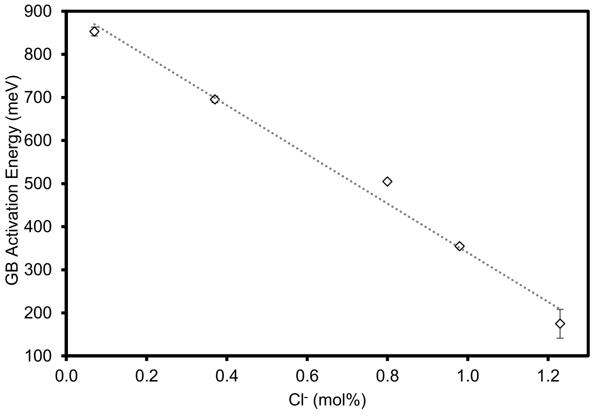

Fig. 9. Estimated activation energy for conduction plotted against the total amount of Cl^- doping in ZnO nanoparticles.

electronic, with electrons as the main charge carriers. This behavior has been associated with the formation of electron donor levels due to the ionization processes that form oxygen vacancies and zinc interstitials [11,62]. Ionic conductivity has been reported for ZnO at higher temperatures (475–550 °C), where the charge carriers are extrinsic protons (H^+) with a minor or insignificant contribution from O^{2-} conduction [63]. Because ionic conductivity is a thermally activated phenomenon, and the E_a at 475–550 °C is ~700 eV [63], at the measured temperatures (100–200 °C), the E_a for ionic conductivity would be considerably greater than that for electronic conductivity, and the latter phenomena would prevail.

4. Conclusions

Cl^--doped ZnO nanoparticles were successfully synthesized using the polymeric precursor method. Wurtzite was the only ZnO phase identified, and the amount of Cl^- retained in the samples was reduced owing to evaporation during calcination. The remaining Cl^- in the samples was quantified using a Cl^--selective electrode, yielding concentrations of 0.1, 0.4, 0.8, 1.0, and 1.2 mol%. The location of the dopant in the ZnO nanoparticles was determined using the selective lixiviation method. The experiment revealed that most of the chloride was on the surface of the ZnO nanoparticles, with a considerable fraction (14%–31%) located in the GBs. Impedance spectroscopy measurements showed a significant decrease in the total electrical resistivity. From this, an increase in the total electrical conductivity agreed with the amount of Cl^- segregated at the GBs. The electric potential barrier associated with the depletion layer at the GBs was reduced by 595 meV, and the activation energy for conduction was reduced by 685 meV as the amount of Cl^- increased. The data suggest that the increase in the total electrical conductivity was caused by the segregation of Cl^- at the GBs rather than an increase in charge carriers in the bulk.

Declaration of competing interest

The authors declare that they have no known competing financial interests or personal relationships that could have appeared to influence the work reported in this paper.

Acknowledgments

We gratefully acknowledge the support of the Research Centre for Gas Innovation (RCGI), hosted by the University of São Paulo (USP) and sponsored by the São Paulo Research Foundation (FAPESP, 2014/50279-4 and 2019/10109-6) and Shell Brazil, and the strategic importance of the support provided by the ANP (Brazil's National Oil, Natural Gas, and Biofuels Agency) through the R&D levy regulation. FCF acknowledges for the partial funding of the Center for Innovation on New Energies (CINE) Shell (ANP) / FAPESP (2017/11937-4). DG and FCF are CNPq fellows.

References

[1] Y. Kajikawa, Effects of potential barrier height and its fluctuations at grain boundaries on thermoelectric properties of polycrystalline semiconductors, J. Appl. Phys. 114 (5) (2013), 053707.
[2] M.H. Chowdhury, M.Z. Kabir, Electrical properties of grain boundaries in polycrystalline materials under intrinsic or low doping, J. Phys. Appl. Phys. 44 (1) (2010), 015102.
[3] G.n. Harbeke, Polycrystalline Semiconductors : Physical Properties and Applications: Proceedings of the International School of Materials Science and Technology at the Ettore Majorana Centre, Erice, Italy, 1985. July 1-15, 1984.
[4] J. He, Metal Oxide Varistors from Microstructure to Macro-Characteristics, Wiley-VCH Verlag GmbH & Co. KGaA, Weinheim, Germany, 2019.
[5] D.R. Clarke, Varistor ceramics, J. Am. Ceram. Soc. 82 (3) (1999) 485–502.
[6] R. Long, J. Liu, O.V. Prezhdo, Unravelling the effects of grain boundary and chemical doping on electron–hole recombination in CH3NH3PbI3 perovskite by time-domain atomistic simulation, J. Am. Chem. Soc. 138 (11) (2016) 3884–3890.
[7] M.K. Nowotny, Solid State Chemistry and Photocatalysis of Titanium Dioxide : Special Topic Volume with Invited Peer Reviewed Papers Only, TransTech Publ, Stafa-Zuerich, 2010.
[8] U. Ozgur, Y.I. Alivov, C. Liu, A. Teke, M.A. Reshchikov, S. Dogan, V. Avrutin, S. J. Cho, H. Morko, A comprehensive review of ZnO materials and devices, J. Appl. Phys. 98 (4) (2005).
[9] Y.-M. Chiang, D.P. Birnie, W.D. Kingery, S. Newcomb, Physical Ceramics : Principles for Ceramic Science and Engineering, Wiley, Chichester, 1997.
[10] J. Lee, J.H. Hwang, J.J. Mashek, T.O. Mason, A.E. Miller, R.W. Siegel, Impedance spectroscopy of grain boundaries in nanophase ZnO, J. Mater. Res. 10 (9) (1995) 2295–2300.
[11] J.C. Simpson, J.F. Cordaro, Characterization of deep levels in zinc oxide, J. Appl. Phys. 63 (5) (1988) 1781–1783.
[12] S.S. Li, Semiconductor Physical Electronics, Plenum, New York, 1993.
[13] C. Wöll, The chemistry and physics of zinc oxide surfaces, Prog. Surf. Sci. 82 (2) (2007) 55–120.
[14] M. Watanabe, Photosynthesis of methanol and methane from CO2 and H2O molecules on a ZnO surface, Surf. Sci. 279 (3) (1992) L236–L242.
[15] A. Yildiz, B. Kayhan, B. Yurduguzel, A.P. Rambu, F. Iacomi, S. Simon, Ni doping effect on electrical conductivity of ZnO nanocrystalline thin films, J. Mater. Sci. Mater. Electron. 22 (9) (2011) 1473.
[16] T. Serin, A. Yildiz, Ş. Uzun, E. Çam, N. Serin, Electrical conduction properties of In-doped ZnO thin films, Phys. Scripta 84 (2011), 065703.
[17] A. Yildiz, B. Yurduguzel, B. Kayhan, G. Calin, M. Dobromir, F. Iacomi, Electrical conduction properties of Co-doped ZnO nanocrystalline thin films, J. Mater. Sci. Mater. Electron. 23 (2) (2012) 425–430.
[18] L. Gong, J. Lu, Z. Ye, Transparent conductive Ga-doped ZnO/Cu multilayers prepared on polymer substrates at room temperature, Sol. Energy Mater. Sol. Cell. 95 (7) (2011) 1826–1830.
[19] C.-Y. Tsay, H.-C. Cheng, Y.-T. Tung, W.-H. Tuan, C.-K. Lin, Effect of Sn-doped on microstructural and optical properties of ZnO thin films deposited by sol–gel method, Thin Solid Films 517 (3) (2008) 1032–1036.
[20] F. Wang, J.-H. Seo, Z. Li, A.V. Kvit, Z. Ma, X. Wang, Cl-doped ZnO nanowires with metallic conductivity and their application for high-performance photoelectrochemical electrodes, ACS Appl. Mater. Interfaces 6 (2) (2014) 1288–1293.
[21] K. Gautam, I. Singh, P.K. Bhatnagar, K.R. Peta, Role of Cl doping on the growth and relaxation dynamics of ZnO nanorods synthesized by hydrothermal method, Chem. Phys. Lett. 662 (2016) 196–200.
[22] Y. Zhang, C. Liu, J. Liu, J. Xiong, J. Liu, K. Zhang, Y. Liu, M. Peng, A. Yu, A. Zhang, Y. Zhang, Z. Wang, J. Zhai, Z.L. Wang, Lattice strain induced remarkable enhancement in piezoelectric performance of ZnO-based flexible nanogenerators, ACS Appl. Mater. Interfaces 8 (2) (2016) 1381–1387.
[23] A. Jiamprasertboon, M.J. Powell, S.C. Dixon, R. Quesada-Cabrera, Abdullah M. Alotaibi, Y. Lu, A. Zhuang, S. Sathasivam, T. Siritanon, I.P. Parkin, C.J. Carmalt, Photocatalytic and electrically conductive transparent Cl-doped ZnO thin films via aerosol-assisted chemical vapour deposition, J. Mater. Chem. 6 (26) (2018) 12682–12692.
[24] C. Liu, A. Yu, M. Peng, M. Song, W. Liu, Y. Zhang, J. Zhai, Improvement in the piezoelectric performance of a ZnO nanogenerator by a combination of chemical doping and interfacial modification, J. Phys. Chem. C 120 (13) (2016) 6971–6977.
[25] A.L. da Silva, D.N.F. Muche, L.B. Caliman, J. Bettini, R.H.R. Castro, A. Navrotsky, D. Gouvêa, TiO2 surface engineering to improve nanostability: the role of interface segregation, J. Phys. Chem. C 123 (8) (2019) 4949–4960.
[26] P.A. Lessing, Mixed-cation oxide powders via polymeric precursors, Am. Ceram. Soc. Bull. 68 (5) (1989) 1002–1007.
[27] D. Gouvêa, D.C.C. do Rosário, L.B. Caliman, Surface and grain-boundary excess of ZnO-doped SnO2 nanopowders by the selective lixiviation method, J. Am. Ceram. Soc. 100 (9) (2017) 4331–4340.
[28] H. Gandelman, A.L. da Silva, L.B. Caliman, D. Gouvêa, Surface and grain boundary excess of ZnO-doped TiO2 anatase nanopowders, Ceram. Int. 44 (10) (2018) 11390–11396.
[29] A.A. Bernardes, L.B. Caliman, A.L. da Silva, J. Bettini, K.L. Guimarães, D. Gouvea, Li2O-doped MgAl2O4 nanopowders: energetics of interface segregation, J. Am. Ceram. Soc. 103 (4) (2020) 2835–2844.
[30] A.L. da Silva, L. Wu, L.B. Caliman, R.H.R. Castro, A. Navrotsky, D. Gouvêa, Energetics of CO2 and H2O adsorption on alkaline earth metal doped TiO2, Phys. Chem. Chem. Phys. 22 (27) (2020) 15600–15607.
[31] F.C. Fonseca, R. Muccillo, Impedance spectroscopy analysis of percolation in (yttria-stabilized zirconia)-yttria ceramic composites, Solid State Ionics 166 (1–2) (2005) 157–165.
[32] R.H.R. Castro, D. Gouvêa, Sintering and nanostability: the thermodynamic perspective, J. Am. Ceram. Soc. 99 (4) (2016) 1105–1121.
[33] A.W. Searcy, J.W. Bullard, Thermodynamics and kinetics of surface area changes of faceted particles, J. Am. Ceram. Soc. 77 (9) (1994) 2314–2318.
[34] Y.-M. Chiang, D.P. Birnie, W.D. Kingery, Physical Ceramics: Principles for Ceramic Science and Engineering, John Wiley & Sons, USA, 1997. The MIT Series in Materials Science and Engineering.
[35] D. Gouvêa, D.C.C. Rosário, L.B. Caliman, *Surface and grain-boundary excess of ZnO-doped SnO_2 nanopowders by the selective lixiviation method*, J. Am. Ceram. Soc. 100 (9) (2017) 4331–4340.
[36] D. Gouvêa, R.H.R. Castro, Sintering: the role of interface energies, Appl. Surf. Sci. 217 (1) (2003) 194–201.
[37] D. Gouvêa, G.J. Pereira, L. Gengembre, M.C. Steil, P. Roussel, A. Rubbens, P. Hidalgo, R.H.R. Castro, Quantification of MgO surface excess on the SnO2

nanoparticles and relationship with nanostability and growth, Appl. Surf. Sci. 257 (9) (2011) 4219–4226.

[38] G.J. Pereira, R.H.R. Castro, P. Hidalgo, D. Gouvêa, Surface segregation of additives on SnO2 based powders and their relationship with macroscopic properties, Appl. Surf. Sci. 195 (1) (2002) 277–283.

[39] R.H.R. Castro, G.J. Pereira, D. Gouvêa, Surface modification of SnO2 nanoparticles containing Mg or Fe: effects on sintering, Appl. Surf. Sci. 253 (10) (2007) 4581–4585.

[40] L. Wu, S. Dey, M. Gong, F. Liu, R.H.R. Castro, Surface segregation on manganese doped ceria nanoparticles and relationship with nanostability, J. Phys. Chem. C 118 (51) (2014) 30187–30196.

[41] R.H.R. Castro, Overview of conventional sintering, in: R. Castro, K. van Benthem (Eds.), Sintering: Mechanisms of Convention Nanodensification and Field Assisted Processes, Springer Berlin Heidelberg, Berlin, Heidelberg, 2013, pp. 1–16.

[42] R. Kirchheim, Reducing grain boundary, dislocation line and vacancy formation energies by solute segregation. I. Theoretical background, Acta Mater. 55 (15) (2007) 5129–5138.

[43] R. Kirchheim, Reducing grain boundary, dislocation line and vacancy formation energies by solute segregationII. Experimental evidence and consequences, Acta Mater. 55 (15) (2007) 5139–5148.

[44] A.S. Barnard, P. Zapol, A model for the phase stability of arbitrary nanoparticles as a function of size and shape, J. Chem. Phys. 121 (9) (2004) 4276–4283.

[45] P.M. Diehm, P. Ágoston, K. Albe, Size-dependent lattice expansion in nanoparticles: reality or anomaly? ChemPhysChem 13 (10) (2012) 2443–2454.

[46] E. Chikoidze, M. Nolan, M. Modreanu, V. Sallet, P. Galtier, Effect of chlorine doping on electrical and optical properties of ZnO thin films 516 (2008) 8146–8149.

[47] A. Renaud, L. Cario, X. Rocquefelte, P. Deniard, E. Gautron, E. Faulques, T. Das, F. Cheviré, F. Tessier, S. Jobic, Unravelling the origin of the giant Zn deficiency in wurtzite type ZnO nanoparticles, Sci. Rep. 5 (1) (2015) 12914.

[48] S.C. Abrahams, J.L. Bernstein, Remeasurement of the structure of hexagonal ZnO, Acta Crystallogr. B 25 (7) (1969) 1233–1236.

[49] C.-H. Chang, S. Dey, R.H.R. Castro, Energetics of oriented attachment of Mn-doped SnO2 nanoparticles, J. Phys. Chem. C 119 (35) (2015) 20662–20672.

[50] R. Razavi, M.R. Loghman-Estarki, M. Farhadi-Khouzani, Synthesis and characterization of ZnO nanostructures by polymeric precursor route, Acta Phys. Pol., A 121 (2012) 98–100.

[51] J. Weissmüller, Alloy effects in nanostructures, Nanostruct. Mater. 3 (1) (1993) 261–272.

[52] R.H.R. Castro, On the thermodynamic stability of nanocrystalline ceramics, Mater. Lett. 96 (2013) 45–56.

[53] R.H.R. Castro, Interfacial energies in nanocrystalline complex oxides, Curr. Opin. Solid State Mater. Sci. 25 (3) (2021) 100911.

[54] T. Asokan, R. Freer, Grain and grain boundary conduction in zinc oxide varistors before and after DC degradation, J. Eur. Ceram. Soc. 11 (6) (1993) 545–550.

[55] A. Lasia, Electrochemical Impedance Spectroscopy and its Applications, Springer, New York, 2014 [etc.].

[56] S.A. Ansari, A. Nisar, B. Fatma, W. Khan, A.H. Naqvi, Investigation on structural, optical and dielectric properties of Co doped ZnO nanoparticles synthesized by gel-combustion route, Mater. Sci. Eng., B 177 (5) (2012) 428–435.

[57] W.D. Callister, D.G. Rethwisch, Materials Science and Engineering : an Introduction, John Wiley, Hoboken, NJ, 2009.

[58] D.C. Reynolds, C.W. Litton, T.C. Collins, Some optical properties of group II–VI semiconductors (II), Phys. Status Solidi 12 (1) (1965) 3–55.

[59] J.L. Baptista, P.Q. Mantas, High temperature characterization of electrical barriers in ZnO varistors*, J. Electroceram. 4 (1) (2000) 215–224.

[60] R.W. Major, A.E. Werner, C.B. Wilson, F.A. Modine, Polarization currents in zinc oxide varistors from 77 to 450 K, J. Appl. Phys. 76 (11) (1994) 7367–7371.

[61] L.B. Caliman, R. Bouchet, D. Gouvea, P. Soudant, M.C. Steil, Flash sintering of ionic conductors: the need of a reversible electrochemical reaction, J. Eur. Ceram. Soc. 36 (5) (2016) 1253–1260.

[62] U. Godavarti, V.D. Mote, M. Dasari, Role of cobalt doping on the electrical conductivity of ZnO nanoparticles, Journal of Asian Ceramic Societies 5 (4) (2017) 391–396.

[63] C. Xia, Z. Qiao, C. Feng, J.-S. Kim, B. Wang, B. Zhu, Study on zinc oxide-based electrolytes in low-temperature solid oxide fuel cells, Materials 11 (1) (2017) 40.